Chemical Engineering Journal 514 (2025) 163348

Contents lists available at ScienceDirect

Chemical Engineering Journal

journal homepage: www.elsevier.com/locate/cej

Electrodeposited $BiVO_4$-based photoanodes for an energy-efficient photo-assisted CO_2-to-formate conversion☆

José Antonio Abarca [a,*], Martí Molera [b], Ivan Merino-Garcia [a], Guillermo Díaz-Sainz [a], Angel Irabien [a], José Solla-Gullón [c], Cristian Fàbrega [b], Teresa Andreu [b], Jonathan Albo [a,*]

[a] Departamento de Ingenierías Química y Biomolecular, Universidad de Cantabria, Avenida de los Castros s/n, 39005 Santander, Spain
[b] Institut de Nanociència i Nanotecnologia, Universitat de Barcelona / IN2UB. c/Martí i Franquès, 1, Barcelona 08028, Spain
[c] Institute of Electrochemistry, University of Alicante, Apdo. 99, 03080 Alicante, Spain

ARTICLE INFO

Keywords:
CO_2 photoelectroreduction
$BiVO_4$ photoanodes
Electrodeposition
Formate
Energy efficiency

ABSTRACT

The development of efficient photoanodes that reduce external energy requirements for the electrochemical conversion of CO_2 to formate is essential for the future implementation of this technology. In this work, we explore different photoanode structures based on electrodeposited $BiVO_4$ onto transparent FTO substrates to achieve a more efficient PEC reduction of CO_2. Among the tested structures, the photoanode incorporating a Bi_2O_3 underlayer, which enhances the $BiVO_4$-FTO interface by reducing electron-hole recombination, exhibits the best PEC performance. Integrating this photoanode into a CO_2 photoelectrolyzer with back visible light illumination achieves an impressive current density of -29 mA cm^{-2} at constant -1.8 V (vs. Ag/AgCl). Using a Bi/C GDE as the cathode, the system produces up to 56.2 g L^{-1} of formate with a Faradaic efficiency of 96 %. In terms of energy performance, illuminating the photoanode reduces energy consumption by nearly 40 %, bringing it down to 317 kWh $kmol^{-1}$, with an energy efficiency of 38 %. The external bias can be further decreased by increasing the irradiation intensity to 2.5 suns using concentrated solar light, resulting in an additional 10 % reduction in energy consumption (290 kWh $kmol^{-1}$), while maintaining high conversion efficiencies for CO_2 to formate (over 95 % Faradaic efficiency). Besides, energy efficiency improves by 12 %, as the cathodic potential is reduced to -1.65 V (vs. Ag/AgCl). These results represent significant progress in reducing the external bias required for CO_2 to formate conversion in PEC systems, marking a step toward the industrial application of CO_2 conversion technology.

1. Introduction

The rise in CO_2 emissions from sectors such as energy, industry, and transportation has increased atmospheric CO_2 concentration to over 420 ppm, necessitating urgent decarbonization strategies [1]. While renewable energy generation and industrial electrification are key approaches, some industrial activities require advanced alternatives like carbon capture, utilization, and storage (CCUS) [2].

Among CO_2 utilization methods, electrochemical conversion into value-added products is a promising approach, enabling CO_2 recycling, circular economy integration, and energy storage in chemical bonds [3]. CO_2 electroreduction to formate/formic acid is particularly advanced, with applications in industries such as leather tanning, animal feed, and pharmaceuticals [3,4]. Key performance indicators (KPIs) for industrial viability include high current densities (200 mA cm^{-2}), high formate concentrations (above 21 % wt.), and low energy consumption (below 100 kWh per kmol of formate) [4].

In this regard, gas phase operation at the cathode, where a humified CO_2 stream is fed, has demonstrated its potential to reach high formate concentrations (over 30 % wt.) at high current densities [5]. However, one of the main challenges is the high overpotential required to break the stable C-O bonds in the CO_2 molecule, which directly increases the overall energy consumption [6]. Moreover, the oxidation reaction occurring at the anode significantly impacts the system's energy consumption. In the case of the Oxygen Evolution Reaction (OER), the energy allocated to this reaction can represent up to 90 % of the external energy input [7].

One of the most promising strategies for decreasing energy

☆ This article is part of a special issue entitled: 'ISCRE 28' published in Chemical Engineering Journal.

* Corresponding authors.
E-mail addresses: joseantonio.abarca@unican.es (J.A. Abarca), jonathan.albo@unican.es (J. Albo).

https://doi.org/10.1016/j.cej.2025.163348

Available online 3 May 2025

consumption in the anodic compartment is combining the electrochemical process with the irradiation of a photoactive surface in the anodic compartment (photoanode), thereby harnessing solar energy as a renewable energy source. Switching to a photoelectrochemical (PEC) system with illumination on the anodic surface reduces OER energy requirements and overall consumption, thus improving electron availability at the cathode for a more energy-efficient CO_2 reduction [8,9].

A typical PEC reactor consists of two independent electrodes: the anode and the cathode, which are separated by an ion exchange membrane [10]. This membrane avoids the re-oxidation of the reduction products and facilitates the charge species flow [11].

Among the different PEC electrolyzer configurations [10], the photoanode-cathode (dark) configuration simplifies the reaction mechanism and the overall operation where the photoanode has two main functions: (i) providing an extra electron flux to the cathode by exciting electrons from the valence to the conduction band of the n-type semiconductor upon illumination, which are then transported to the cathode by the external electrical circuit [12], and (ii) promoting the oxidation reaction, usually water oxidation, which supplies the protons and electrons needed for the CO_2 reduction reaction [13,14]. Despite the promising outcomes of PEC electrolyzers for CO_2 reduction, further research efforts must be made to increase the operating current density to close the gap with industrial implementation, as most reported studies operate below industrially relevant current densities [10].

$BiVO_4$ is particularly noteworthy for its OER applications due to its favorable band alignment with water redox levels and activity under visible light irradiation [8]. Besides, $BiVO_4$ is non-toxic, stable, and inexpensive, and has a narrow bandgap (2.4–2.7 eV) [15]. However, several challenges must be tackled in the broader implementation of $BiVO_4$ surfaces in PEC applications, including the stability of the photoelectrodes, which is dependent on the anolyte pH, the attainable current densities, and the onset potential [16], which currently do not meet the requirements for long-lasting electrodes with high current densities.

Moreover, Transparent Conductive Oxides (TCOs) have gained importance as supports for depositing thin films that serve as photoelectrodes [17]. These substrates allow the electrode to be illuminated from both sides. Fluorinated Tin Oxide (FTO) is a competitive TCO substrate due to its low cost and stability [18]. Additionally, the use of these substrates allows for higher current densities compared to carbon-based photoanodes [19,20], which expands the range of CO_2 reduction products that can be obtained. Carrera-Crespo et al. [21] evaluated the combination of FTO with a $BiVO_4$ thin film and examined the effects of illumination on photoelectrode performance. They found that back-illumination operation led to an improved PEC activity, as front-illumination is hindered by the $BiVO_4$ layer blocking light transfer to the substrate, thereby limiting electron generation in the FTO [18]. Nevertheless, FTO becomes activated when the photoanode is back-illuminated, enhancing the PEC activity of the FTO-$BiVO_4$ junction.

Electron-hole pairs are generated within the light's maximum penetration depth, electrons then move towards the FTO-$BiVO_4$ interface, while holes are transported to the electrolyte interface [22]. However, the rate of charge transfer is lower for electrons passing through the FTO-$BiVO_4$ interface due to the electronic structure of the catalyst [22]. This leads to electron accumulation, making them prone to recombination with unpaired holes [23]. The interaction between the FTO and the $BiVO_4$ thin film is therefore crucial for the PEC activity of the photoanodes [24]. Different strategies have been proposed to modify the FTO-$BiVO_4$ interface to reduce charge recombination and improve PEC activity [24–27]. One promising approach is placing a metal oxide layer between the FTO and $BiVO_4$ thin film. This acts as a "hole mirror", preventing holes from reaching recombination centers at the FTO-$BiVO_4$ interface [22,28]. It also maintains the $BiVO_4$ band-bending, enhancing the catalyst's capability to carry out the OER. Bi_2O_3 is an efficient metal oxide for improving the FTO-$BiVO_4$ interface, as oxygen vacancies in the heterostructure formed by Bi_2O_3 and $BiVO_4$ improve the separation of the generated electron-hole pairs [29,30]. The more positive valence and conduction band levels of the Bi_2O_3 shift electrons from $BiVO_4$ to Bi_2O_3, directing them to the electron collector (FTO substrate), while unpaired holes migrate to the electrolyte interface to carry out the OER [31].

Furthermore, the method used to fabricate $BiVO_4$ thin films on the FTO substrate can also impact the electron transfer to the current collector. A homogeneous deposition of the catalyst, avoiding particle agglomeration, ensures close contact at the FTO-$BiVO_4$ interface [32], thus enhancing electron transfer and minimizing electrical resistance. Electrodeposition is particularly notable for its simplicity, ability to produce highly homogeneous and stable catalyst thin films, and versatility, allowing the fabrication of photoanodes in almost any morphology [33]. This electrically driven process involves depositing metal ions from an electrolyte onto the FTO substrate surface to form a thin photoactive film.

All in all, this work presents the preparation and application of $BiVO_4$-based photoanodes, which are active under visible light, for energy-efficient PEC solar-driven CO_2 reduction to formate in the gas phase. The $BiVO_4$-based photoanodes, in which the OER takes place, are engineered and fabricated through electrodeposition and integrated into a photoelectrolyzer that utilizes a transparent FTO substrate as the electron collector, allowing for back-illumination of the photoelectrode. Different strategies are used to optimize PEC activity [34], including modifications to the thickness of the thin $BiVO_4$ film and incorporating a metal oxide interlayer (Bi_2O_3) to improve electron-hole separation. Concentrated solar light is then used to enhance the system's energy efficiency by reducing the external bias needed for PEC CO_2 reduction to formate. The design and development of the improved photoanode structures, as well as the optimization of operational conditions for these photoanodes, enable operation at higher current densities, bridging the gap toward achieving industrially relevant conditions for PEC CO_2 electrolyzer operation. This advancement has the potential to facilitate the large-scale implementation of integrated PEC solutions driven by sunlight, thereby improving the sustainability and energy efficiency of CO_2 conversion systems.

2. Methodology

2.1. (Photo)electrodes fabrication

The photoanodes are fabricated with a geometric area of 10 cm^2. To synthesize the $BiVO_4$ electrodes, different electrodeposition methods followed by thermal treatment are employed, as shown in Fig. 1.

The electrochemical bath is prepared by dissolving 0.97 g of Bi $(NO_3)_3$ and 3.32 g of KI in 50 mL of MiliQ water. Then, 0.5 g of p-benzoquinone is dissolved in 20 mL of ethanol and mixed with the previous solution. In the first electrodeposition step, BiOI is electrodeposited onto FTO-glass substrates by applying two potentiostatic pulses, the first at −0.35 V vs. Ag/AgCl/KCl (3.5 M) for 1 min, followed by a second pulse at −0.1 V vs. Ag/AgCl/KCl (3.5 M) for 3 min, using a Biologic VSP300 potentiostat. Then, the BiOI electrodes are cleaned with deionized water and air-dried.

To synthesize Photoanode A, a vanadium precursor solution (0.2 M vanadyl acetylacetonate in DMSO solvent) is spray-coated onto the electrodes while heating. Then, thermal treatment is applied at 450 °C for 2 h with a heating ramp of 2 °C min^{-1}. After cooling, excess V_2O_5 is removed by cleaning the electrodes with a 1 M KOH solution for 3 min, followed by rinsing with water and air-drying.

To synthesize Photoanode B, additional electrodeposition of BiOI is done before the addition of vanadium precursor and thermal treatment.

For the synthesis of Photoanode C, a thermal treatment without vanadium is applied at 550 °C for 2 h. Then, a second BiOI layer is electrodeposited, and the vanadium precursor is applied, followed by thermal treatment at 450 °C.

A bismuth (Bi)-based gas diffusion electrode (GDE) is employed as a

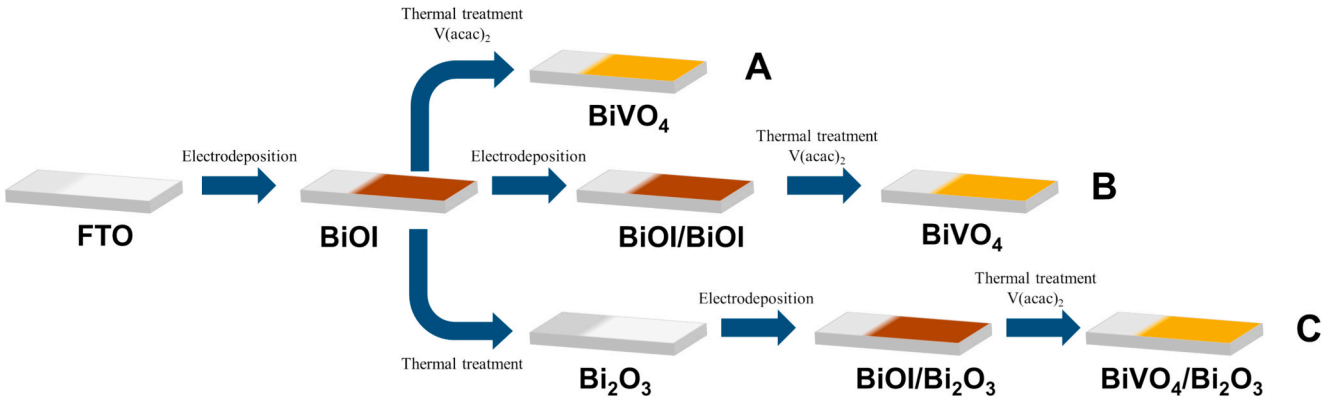

Fig. 1. Schematic representation of the steps followed in the fabrication of the different tested $BiVO_4$-based photoanodes.

dark cathode to facilitate the use of gas-phase reactants, such as CO_2, by maintaining high concentrations within the reaction zone and enabling operation at high current densities [35]. Carbon-supported Bi nanoparticles (Bi/C) [5] are selected as the electrocatalyst due to their high selectivity for producing formate during the CO_2 reduction reaction [3]. The electrocatalyst is deposited onto carbonaceous support to form a GDE, which consists of two distinct layers: (i) a gas diffusion layer (GDL), composed of a carbon paper substrate and a microporous layer (Sigracet 39 BB, Fuel Cell Store) to enhance CO_2 mass transfer to the catalyst, and (ii) the catalyst layer, which is produced through an automated spray pyrolysis technique [36]. In this process, a catalytic ink, comprising Bi/C nanoparticles, isopropanol (laboratory reagent grade, ≥99.5 %, Fisher Chemicals) as the solvent, and Nafion D-521 (5 % wt dispersion, Ion Power) as a binder, is sprayed onto the GDL to achieve a catalyst loading of 0.75 mg cm^{-2}, representing the optimal best trade-off between formate concentration and minimal catalyst amount usage [5].

2.2. Physicochemical characterization

The photoanodes A, B, and C structural and optical properties are characterized using various techniques. A Field Emission Scanning Electron Microscopy (FESEM) on a JEOL J-7100 coupled with energy dispersive spectroscopy (EDS) is employed to characterize the morphology of the samples. X-ray diffraction (XRD) patterns are determined using a PANalytical X'pert PRO diffractometer with monochromatized Cu Kα radiation (λ = 1.5406 Å), operating at 45 kV and 40 mA in a Bragg-Brentano configuration. UV–vis spectroscopy (UV–vis) is performed on a Lambda 950 UV–vis-NIR spectrometer (PerkinElmer) equipped with a 150 mm Integrating Sphere and Spectralon standard. Transmittance and reflection measurements are carried out separately for each sample over a wavelength range of 100–- 800 nm, with a 5 nm step, and the band gap is determined using a Tauc plot. Raman spectroscopy measurements are carried out using a Jovin Yvon LabRaman HR800 in the 100–1000 cm^{-1} range using a laser with a wavelength of 528 nm and are calibrated with a silicon reference.

The morphology and particle size distribution of the Bi/C electrocatalyst are analyzed using Transmission Electron Microscopy (TEM) with a JEOL JEM-2010 operating at 200 kV and a JEOL JEM-1400 at 120 kV. Additionally, the Bi/C GDEs are examined through powder X-ray diffraction (PXRD) using a Philips X'PERT PRO system at 40 kV and 40 mA. The electrode microstructure is investigated via Scanning Electron Microscopy (SEM) with a JEOL JSM-7000F operating at 10–20 kV, while the distribution of Bi across the GDE is assessed through elemental EDX mapping, performed with a HITACHI S-3000 N SEM equipped with a Bruker Xflash X-ray detector at 20 kV.

2.3. Photoelectrochemical characterization

The PEC characterization is conducted using an adapted filter-press reactor (ElectroCell) with a transparent plate at the anodic compartment (PMMA methacrylate, 92 % transparency). The photoanode surface is irradiated from the back side, to maximize the photocurrent generated [18], using visible light (I_{peak} at 450 nm) from a LED lamp (Photolab LED 365–3/450–3, Apria Systems) with an intensity of 100 mW cm^{-2} at the surface. A platinized-titanium plate electrode (ElectroCell) is employed as the dark cathode for PEC characterization.

An aqueous 0.5 M $KHCO_3$ solution (ACS reagent, Thermo Scientific) is fed to both cathodic and anodic compartments at a constant flowrate of 0.57 mL min^{-1} cm^{-2} as the reaction medium. The slightly alkaline pH (8.7) of the electrolyte helps prevent the chemical degradation of the $BiVO_4$ surfaces. The cell compartments are divided by a Nafion 117 cation exchange membrane (0.180 mm thick, > 0.9 meq g^{-1} exchange capacity, Ion Power) to avoid product crossover between the cathode and photoanode [37]. A leak-free Ag/AgCl 3.4 M KCl electrode serves as the reference electrode in the anode compartment.

Each photoanode is subjected to different PEC tests, including chronoamperometry analyses at a constant voltage of −1.8 V (vs. Ag/AgCl) for 30 min, under on and off illumination. The applied potential is controlled with an Autolab PGSTAT 302 N (Metrohm Hispania) potentiostat. The voltage is chosen as the most suitable for the CO_2 reduction to formate [36]. After determining the photocurrent density for each photoanode, Linear Sweep Voltammetry (LSV) is conducted between −2.2 and −0.8 V (vs. Ag/AgCl), at a scan rate of 10 mV s^{-1} to determine the most suitable potential window under illumination. Electrochemical Impedance Spectroscopy (EIS) is used to determine the electrical resistance, at a constant voltage of −0.8 V (vs. Ag/AgCl) with frequencies ranging between 10 kHz to 0.1 Hz.

2.4. PEC CO_2 reduction performance

The continuous PEC CO_2 reduction is carried out at room temperature and ambient pressure in the same adapted filter-press reactor (ElectroCell), with a Bi/C GDE as the dark cathode (Fig. S.2). The GDE is placed in close contact with the ion exchange membrane to form a Membrane Electrode Assembly (MEA). The cathode compartment is fed with a humified pure CO_2 stream (via home-made bubbler) at a flowrate of 200 mL min^{-1}. Meanwhile, an aqueous anolyte (0.5 M $KHCO_3$) is pumped into the anode compartment at a constant flowrate of 0.57 mL min^{-1} cm^{-2}.

PEC CO_2 reduction tests are carried out by duplicate for 90 min at a constant voltage of −1.8 V (vs. Ag/AgCl), which has been found to be optimal for the selective production of formate [18,36]. The formate produced in the cathode during the experiments is determined by ion chromatography (Dionex ICS 1100, using Na_2CO_3 as eluent with a concentration of 4.5 mM and a flow rate of 1 mL min^{-1}). The relative

standard deviations are below 10 % for the formate concentration determination.

For tests with concentrated solar light, the photoanodes are illuminated by means of a solar simulator (LSH-7320 ABA LED Solar Simulator, Newport). Different light intensities are reached regulating the distance from the light source to the photoactive surface, thus controlling light intensity from 1 to 2.5 suns. To evaluate the photoanode response under solar concentration, continuous CO_2 reduction to formate is carried out at galvanostatic conditions, with a constant current density of −29 mA cm^{-2}. The performance of the PEC system is evaluated by considering the following figures of merit [10,18,36]:

- Formate production rate, *r*, the amount produced at the cathode per unit of geometric area during the experimental period (Eq. 1):

$$r\left(\frac{mol}{m^2 s}\right) = \frac{N_F}{A} \tag{1}$$

Where N_F is the molar flux of formate (mol s^{-1}) and *A* is the cathode geometric area (m^2).

- Faradaic Efficiency, *FE*, selectivity of the external current supplied toward the production of formate (Eq. (2)):

$$FE(\%) = \frac{z \bullet F \bullet N_F}{I} \bullet 100 \tag{2}$$

Where *z* is the number of electrons exchanged, in the case of formate is 2, *F* is the Faraday constant (96 485C mol^{-1}), N_F refers to the molar flux of formate (mol s^{-1}), and *I* is the total current provided to the system (A).

- Energy efficiency, *EE*, portion of the total energy supplied that is harvested in the CO_2 reduction to formate (Eq. (3)):

$$EE(\%) = FE \bullet \frac{E_T}{E_{Cathode}} \tag{3}$$

Where *FE* is the Faradaic Efficiency to formate (%), E_T is the theoretical potential for the CO_2 reduction to formate (−0.68 V vs. Ag/AgCl), and $E_{Cathode}$ is the external voltage supplied to the cell.

- Energy Consumption, *EC*, external energy input required by the PEC system to produce a given quantity of formate (Eq. (4)):

$$EC\left(\frac{kWh}{kmol}\right) = \frac{I \bullet V}{N_F} \tag{4}$$

Where *I* and N_F have the same significance as in Eq. (1) and Eq. (2) and V is the overall cell potential (V).

- Energy-to-fuel conversion efficiency, *ETF*, defined as the chemical energy produced for formate relative to the total energy supplied to the electrochemical cell (Eq. (5)):

$$ETF(\%) = \frac{r_F \bullet \Delta G^0}{P_{External}} \bullet 100 \tag{5}$$

Where r_F is the formate rate (mol s^{-1} m^{-2}), ΔG^0 (J mol^{-1}) is defined as the Gibbs free energy for the conversion of gaseous CO_2 to formate (0.00543 J mol^{-1}), and $P_{External}$ (W cm^{-2}) is the external power density provided to the photoelectrolyzer.

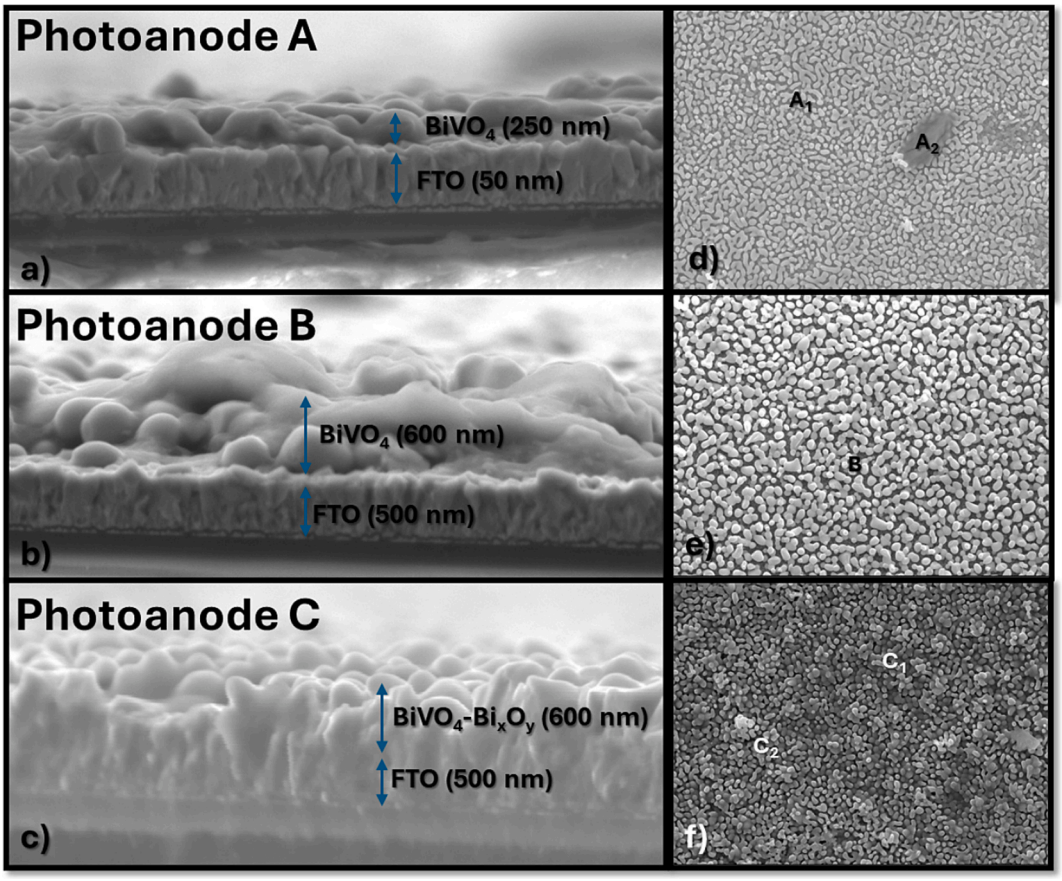

Fig. 2. Cross-section and surface SEM images of the fabricated photoanodes, a) Photoanode A:$BiVO_4$, b) Photoanode B: Thick $BiVO_4$, and c) Photoanode C: $BiVO_4/Bi_2O_3$.

3. Results

3.1. Photoanode characterization

The different $BiVO_4$-based surfaces prepared underwent different electrodeposition processes to coat the FTO transparent substrate, resulting in distinct morphologies and microstructures, as shown in SEM images (Fig. 2).

The cross-sectional images of the photoanodes reveal that the different electrodeposition processes impact the thickness of the $BiVO_4$ layer on the FTO layer. For photoanode A (Fig. 2.a), the thickness is the smallest, approximately 250 nm, as the electrodeposition is only carried out in one cycle. In contrast, the electrodes subjected to two electrodeposition cycles (photoanodes B and C), have a thicker catalyst layer of around 600 nm, as observed in Fig. 2.b and 2.c. However, despite the same thickness, the morphology of the $BiVO_4$ layers differs. Photoanodes A and B present a more homogeneous catalyst distribution, as confirmed by surface SEM analysis in Fig. 2.d-f, although some potassium impurities are detected during fabrication, as indicated by the elemental analysis of points A_1 and A_2 (Table S.1 and Fig. S.1, as shown in the Supporting Information). Photoanode C also displays a homogeneous distribution, but the surface also shows Bi-rich material agglomerations, likely due to the subsequent electrodeposition of $BiVO_4$ over a Bi_2O_3 layer, as indicated in Fig. S.1 and Table S.1.

The alterations in morphology and structure among the photoanodes may influence the photoactivity and surface response under visible illumination [38]. To assess their optical properties, a VIS-absorbance analysis is performed for each photoanode. Fig. 3 shows the absorption spectra and the corresponding Tauc plot to determine the optical bandgap.

The combination of the $BiVO_4$- Bi_2O_3 in the photoanode C forms a heterojunction that improves the optical properties of the photocatalyst [39]. As the Conduction and Valence bands of Bi_2O_3 are positioned lower than those of $BiVO_4$, a Type II heterojunction is formed (Fig. S.1) [40,41]. In this photoanode, Bi_2O_3 acts as an interlayer between the FTO substrate and the active $BiVO_4$ to facilitate charge separation and electron transport to the cathode [29]. This results in an enhancement of the VIS-absorbance spectra (Fig. 3.a), compared to photoanodes A and B, the additional Bi_2O_3 layer beneath the $BiVO_4$ enhances light absorption, particularly above 500 nm, due to the lower bandgap (Fig. 3.b). All three electrodes display an absorption edge at approximately 500 nm, with bandgaps between 2.5 eV for photoanode A, and 2.4 eV for photoanode C, consistent with the absorption edge of $BiVO_4$ powder (506 nm, 2.45 eV) [18].

Fig. 4.a. shows that photoanode C leads to the highest current density reached at the cathode, with –33 mA cm^{-2}, in contrast to photoanodes A and B which reach –22 and −29 mA cm^{-2}, respectively. This fact can be related to the flake-like nanostructures that can improve the charge separation, resulting in enhanced OER activity [42]. Moreover, the Bi_2O_3 layer coated under the $BiVO_4$ acts as "hole mirror" preventing the fast charge recombination near the interface between FTO and $BiVO_4$ [22], allowing more electrons to effectively reach the current collector, and then the cathode through the external circuit. This, along with the higher absorbance shown by photoanode C, supports the results reached in chronoamperometry tests in terms of an enhanced attainable current density. On the other hand, photoanode B results in a better PEC performance in comparison with photoanode A, despite having similar absorbances. In this case, the larger amount of catalyst loading in photoanode B (as seen in Fig. 2) allows more active sites to be light-excited, enlarging the possible electron flux to the cathode, thus resulting in higher photocurrent density [19].

Fig. 4.b reveals that photoanode B presents lower electrical resistance, even though the PEC activity is not favored by this low charge, as discussed before (Fig. 4.a). Photoanode A also presents lower electrical resistance than photoanode C. As previously reported [18], lower electrical resistance does not always favor the PEC activity. For instance, in photoanodes A and B part of the particles deposited may be acting as recombination centers instead of active sites, therefore hindering the overall PEC performance, as there is a high recombination rate while exhibiting low electrical resistance [43]. In agreement with previous literature [18,43], the improved interface of photoanode C improves the hole-electron pair separation, allowing more electrons to reach the cathode, achieving higher current densities despite its higher electrical resistance compared to photoanode B.

3.2. Continuous PEC CO_2 reduction to formate

The fabricated photoanodes are integrated into the filter-press photoelectrolyzer for a more efficient conversion of CO_2 into formate in a gas phase configuration. TEM images reveal a spherical morphology with a narrow particle size distribution of approximately 9.3 nm, as depicted in Fig. S.4 [44]. The morphology of the synthesized GDEs is

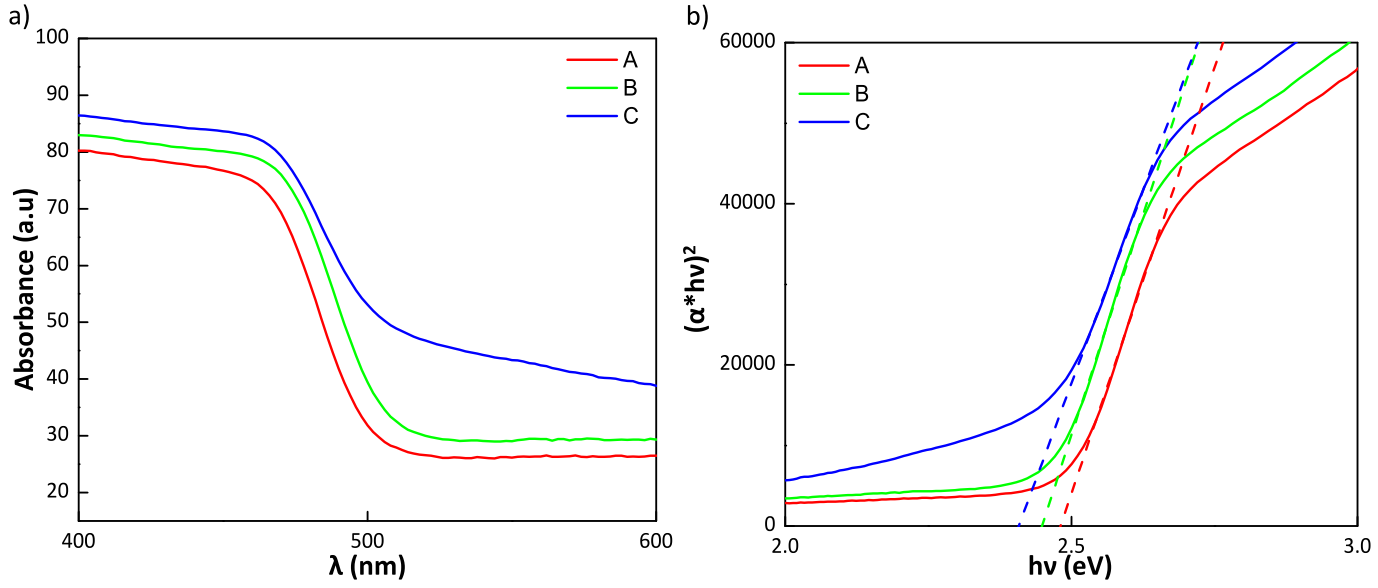

Fig. 3. A) vis-absorbance spectra, and b) tauc plot of the fabricated photoanode. (red line, photoanode a bivo$_4$; Green line, Photoanode B: Thick $BiVO_4$; Blue line, Photoanode C: $BiVO_4/Bi_2O_3$). (For interpretation of the references to colour in this figure legend, the reader is referred to the web version of this article.)

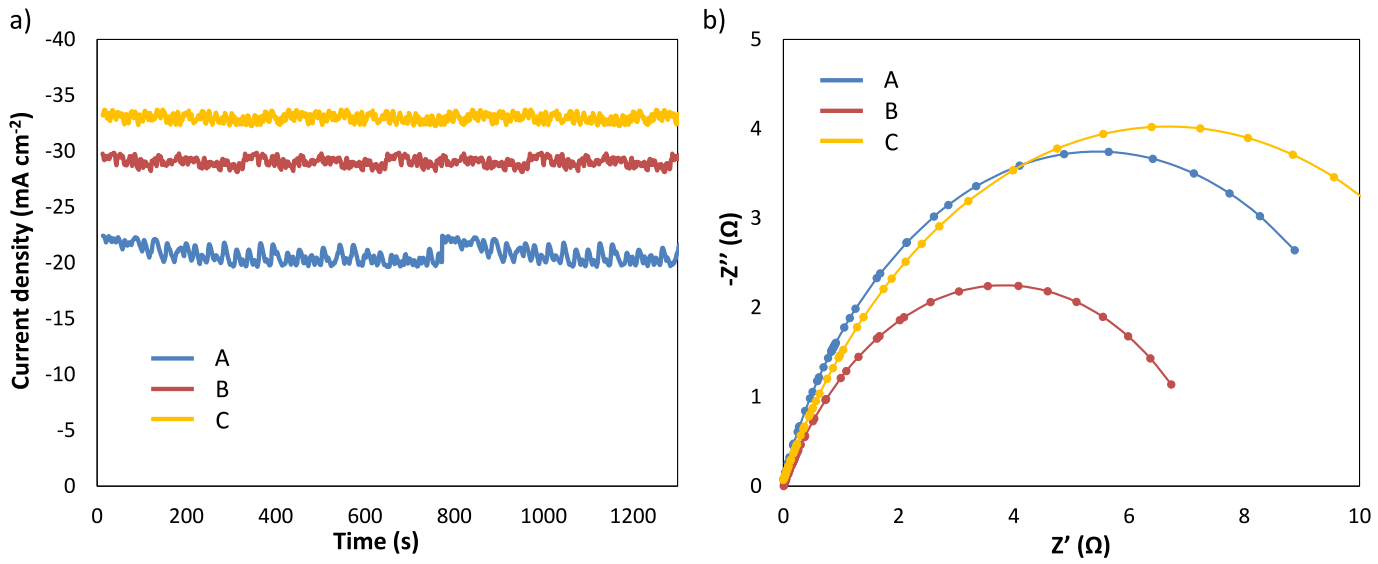

Fig. 4. A) chronoamperometry results at−1.8 V vs. Ag/AgCl, and b) EIS of the electrodeposited photoanodes. (Blue, Photoanode A: $BiVO_4$; Red, Photoanode B: Thick $BiVO_4$; Yellow, Photoanode C: $BiVO_4/Bi_2O_3$). (For interpretation of the references to colour in this figure legend, the reader is referred to the web version of this article.)

further examined through SEM imaging. Top-down SEM and EDX mapping (Fig. S.5) confirm a uniform dispersion of the catalyst across the GDE surface [36,44]. Cross-sectional analysis reveals that the GDE thickness ranges from 275 to 290 μm. Lastly, XRD analysis (Fig. S.6) indicates that the majority of the GDE surface consists of carbon-based materials, with weak Bi-related signals, with weak Bi-related signals, as expected for Bi nanoparticles supported on carbon [36]. Fig. 5 displays the FEs toward formate and the current densities reached under both light and dark conditions as a function of photoanode composition.

Photoanode C demonstrated the best PEC CO_2 reduction performance, as expected based on characterization results. Compared to dark conditions, light exposure increased the current density by 52 % (−29 mA cm^{-2}). This is lower than the current density achieved during the characterization tests, explained by a reduced conductivity in gas phase tests. A similar effect is observed in Photoanodes A and B, where current densities under illumination are –23 and −26 mA cm^{-2}, with an enhancement of 27 % and 44 %, respectively. Therefore, photoanode C, under illumination, exhibited an additional photocurrent of −10 mA

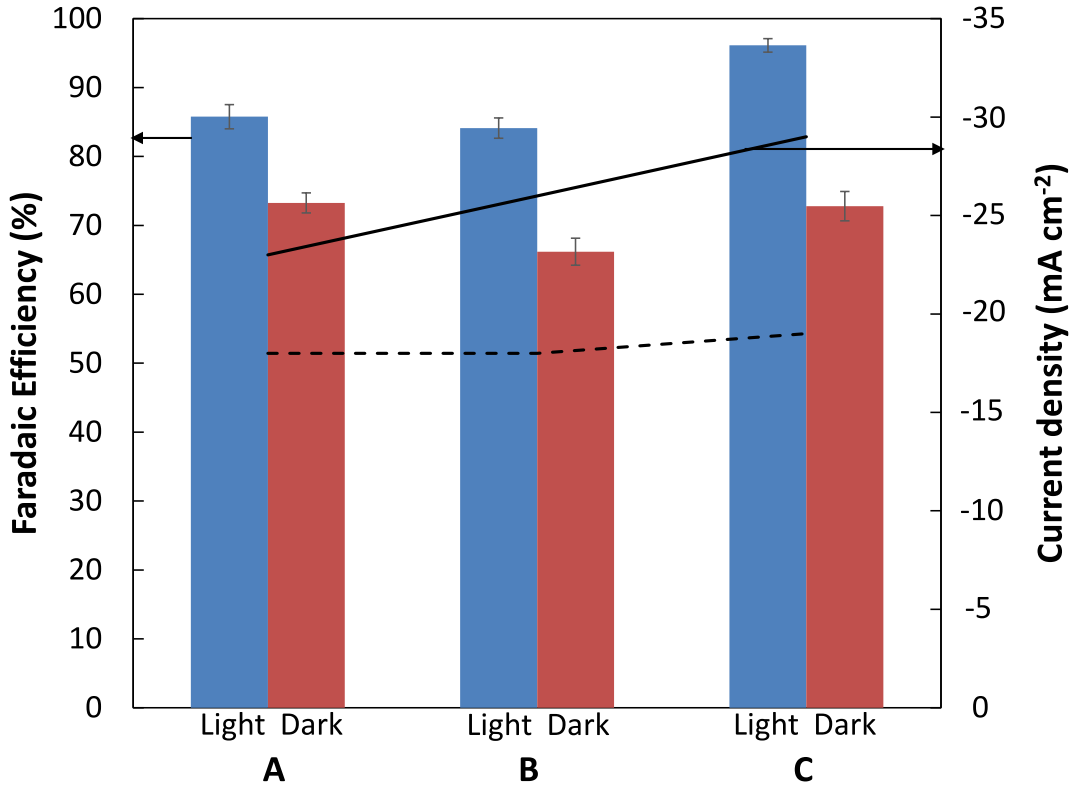

Fig. 5. FE and current density results for continuous CO_2 PEC reduction to formate using different electrodeposited photoanodes at −1.8 V vs. Ag/AgCl, under visible illumination (100 mW cm^{-2}) (A, $BiVO_4$; B, Thick $BiVO_4$; C, $BiVO_4/Bi_2O_3$).

cm^{-2}, associated with an improved electron flow from this photoanode to the cathode. This increased electron availability enhanced the CO_2 reduction reaction at the cathode, producing formate concentrations of up to 59.2 g L^{-1}, which results in a significant improvement in comparison with a concentration of 38.8 g L^{-1} obtained under dark operation.

The light exposure also results in a notable effect on the *FE* toward formate. As observed in Fig. 5, all photoanodes achieved higher *FE*s under illumination, indicating that the extra electron flow is effectively used in the CO_2 reduction to formate. This increase is likely due to improved reaction kinetic from enhanced electron availability at the same applied potential [45]. Photoanode C achieved an outstanding *FE* of 96 % under illumination, representing an increment of 33 % compared to dark operation. Additionally, the formate production rate increased significantly due to enhanced reaction kinetics. The use of photoanode C leads to a formate rate in the cathode of 1.44 mmol m^{-2} s^{-1}, nearly double the 0.77 mmol m^{-2} s^{-1} observed under dark conditions (Table S.2).

Regarding energy consumption, integrating a photoactive surface on the anode reduced overall energy requirements and improved energy efficiency. The effect of irradiating the different photoanodes on energy output is presented in Fig. 6:

As expected, *EC* in the photoelectrolyzer decreased significantly when the photoanodes are illuminated, with a reduction of 30–40 %, linked to the decreased cell potential due to the fact that the anodic potential for the OER is reduced by the illumination. Photoanode C exhibited the best performance under illumination, reducing energy consumption to 317 kWh $kmol^{-1}$, comparable to previous works on PEC CO_2 reduction to formate [18], representing a promising alternative for reducing energy consumption compared to conventional CO_2 electrolyzers, which ranges between 250–300 kWh $kmol^{-1}$ when working at low current densities. In terms of *EE*, there is a marked improvement when using the photoanodes, closely related to the increased *FE*. The amount of the total energy provided to the PEC cell that is used for the CO_2 reduction to formate augments from 23-29 % in dark operation to 32–38 %, under illumination, as the photoelectrocatalytic activity reduces the anode overpotential for the OER [46], making more energy available for the cathode to carry out the reduction of CO_2 to formate. Photoanode C exhibited the highest *EE* among the fabricated photoanodes, reaching up to 38 %, representing a significant advancement in PEC systems and improving upon previous CO_2 reduction to formate reduction studies [18]. Compared to conventional CO_2 electroreduction, these results place energy efficiency among the best reported for formate production [3], with an *EE* in the range of 35–40 %. Furthermore, photoanode C showed the highest energy-to-fuel conversion efficiency, reaching 4.75 %.

Finally, as the stability of the photoanodes is a key aspect in potential PEC electrolyzer applications, fresh and used photoanodes are characterized to study any possible alteration that may have occurred during the OER reaction.

No detachment of catalytic material from any of the photoanode surfaces was observed from SEM (Fig. 7.a), demonstrating the mechanical stability of the electrodeposited catalyst layer. However, post-experiment images revealed salt deposits, primarily related to the formation of carbonate and bicarbonate on the photoanode surface under anodic oxidation conditions. XRD analysis (Fig. 7.b) confirmed the presence of these deposits, identifying them primarily as potassium carbonate (K_2CO_3) and bicarbonate ($KHCO_3$), with some potassium hydroxide (KOH) also detected, consistent with the use of $KHCO_3$ as the anolyte for OER. XRD analysis also confirmed the stability of $BiVO_4$ under reaction conditions, with no significant changes in its crystalline structure before and after the experiments. It should be noted that the XRD spectrum of $BiVO_4/Bi_2O_3$ photoanode does not exhibit any Bi_2O_3 diffraction peaks, likely due to the amorphous nature of the layer. However, Raman analysis is more sensitive to the microstructure and as seen in Fig. S.7, it revealed the presence of Bi-O bonds in $BiVO_4/Bi_2O_3$ that are absent in pure $BiVO_4$ electrodes.

Fig. 8 shows that for Photoanodes A and B, no significant changes in

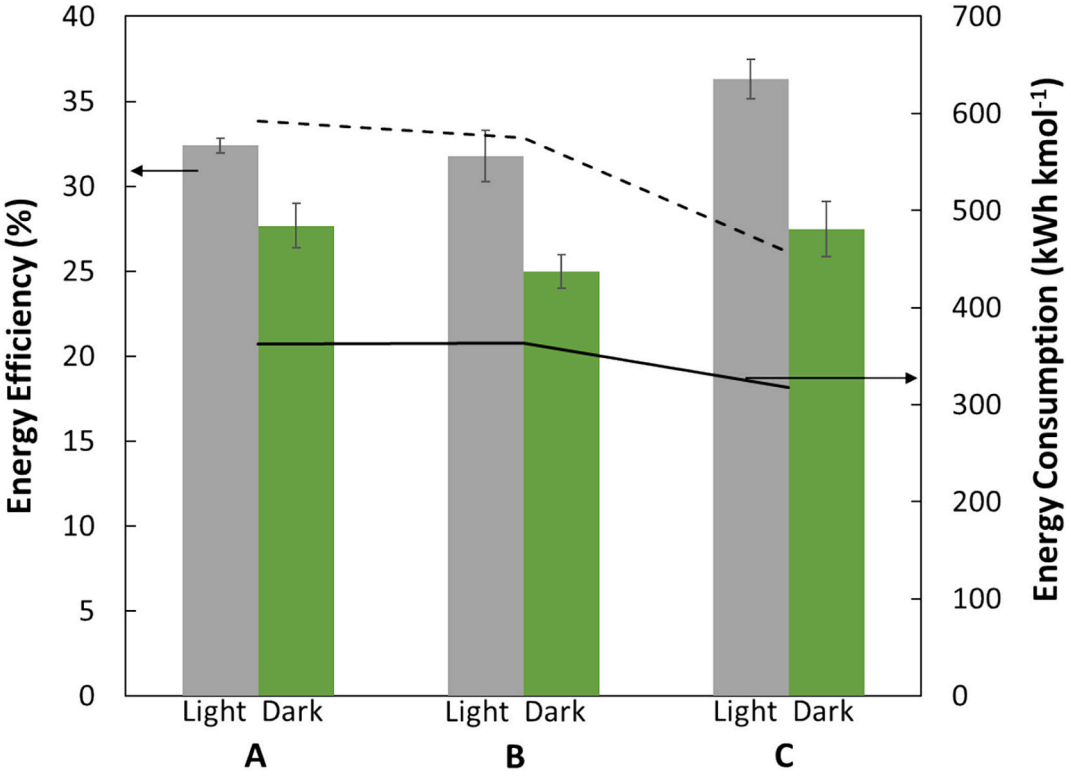

Fig. 6. FE and current density results for the continuous CO_2 PEC reduction to formate using different electrodeposited photoanodes at −1.8 V vs. Ag/AgCl, under visible illumination (100 mW cm^{-2}) (A, $BiVO_4$; B, Thick $BiVO_4$; C, $BiVO_4/Bi_2O_3$).

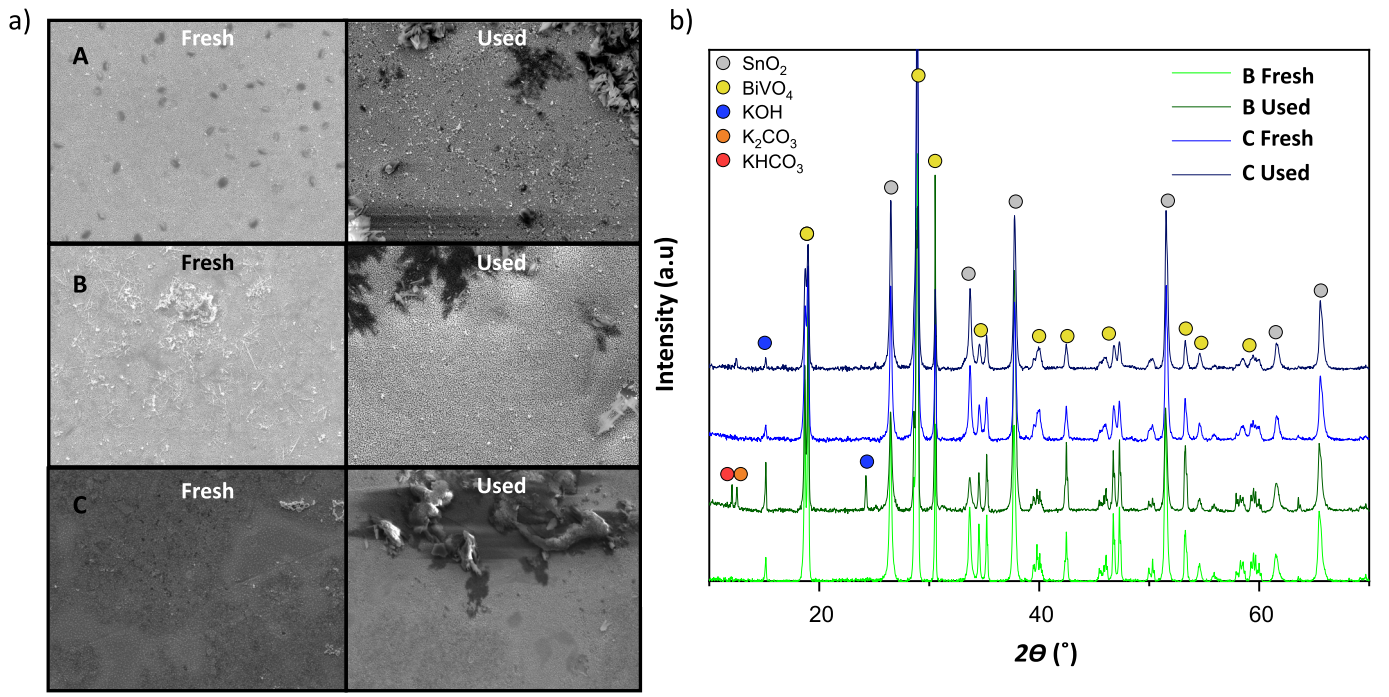

Fig. 7. A) sem images, and b) xrd analysis results of the surface of the different electrodeposited photoanodes before and after experiments. (a, bivo$_4$; B, Thick $BiVO_4$; C, $BiVO_4/Bi_2O_3$).

absorbance were observed before and after the operation. However, photoanode C exhibited a reduction in absorbance, particularly at the absorption edge. This suggests that the behavior of photoanode C can be related to the degradation of the Bi_2O_3 layer, as this photoanode after use showed an absorbance level similar to both photoanodes A and B. Additionally, Raman analysis (Fig. S.8) shows that previously identified Bi-O peaks disappear after use, corroborating the Bi_2O_3 layer degradation. After multiple operational cycles, a decline in the cathodic current density is observed, as shown in Fig. S.9, which might be attributed to a degradation of both dark cathode and photoanode. However, within each cycle, the current density remains stable under illumination. The systems stability is not only influenced by the photoanode, thus the GDE plays an important role, as its deactivation can reduce both the current density and CO_2 reduction performance, mainly due to salt precipitation and electrode flooding [47].

Finally, the use of concentrated solar light is proposed as a strategy to further improve energy efficiency and therefore the overall energy performance of the PEC CO_2 reduction system. It is necessary to consider the various drawbacks that an increase in solar irradiation intensity may generate, such as the saturation of the photocatalyst due to a higher recombination rate, which prevents an increase in intensity from improving the generated current density [48]. Additionally, the temperature rise can affect both the kinetics of the OER and the generation and detachment of O_2 bubbles on the surface of the photoanode [49], which hinders charge separation and reduces the overall efficiency of the system. Furthermore, it must be evaluated whether the improvement in process performance due to the increase in solar intensity compensates for the costs required to implement the auxiliary systems to increase irradiation intensity. In this sense, photoanode C is selected to evaluate the effect of sunlight irradiation, according to the best PEC performance results. Experiments are carried out in galvanostatic conditions at a constant -29 mA cm^{-2}, based on previous results employing this photoanode under 100 mW cm^{-2} of visible light illumination. The focus is paid on the decrease of the energy consumption for formate production and energy efficiency, as depicted in Fig. 9.

The higher photon flux reaching the photoactive surface of the photoanode due to the increased solar irradiation intensity enhances the number of excited active sites, which in turn lowers the overpotential needed for OER [50], and consequently, there is an extra electron flow to the cathode. Lowering the anode overpotential results in a smaller value of cell voltage. The performance of the system for CO_2 reduction to formate remains constant under the operation at -29 mA cm^{-2}, with formate concentrations ranging from 55-60 g L^{-1} and *FE*s between 93–98 % for every solar intensity (Table S.2). The overall energy consumption for formate production is lowered from 318 to 290 kWh kmol^{-1}, thus increasing 2.5 times the solar irradiation achieves almost 10 % reduction in the energy requirements of the system. On the other hand, the cathode potential is also lowered when applying higher solar irradiations, which results in improved energy efficiencies. In the case of working at 2.5 suns intensity, the cathode potential is reduced to -1.65 V (vs. Ag/AgCl), resulting in an *EE* value of 40.9 %, which represents a 12 % increase compared to the baseline case under 100 mW cm^{-2} illumination. In contrast, the *ETF* is reduced from 4.74 % (1 sun) to 4.45 % (2.5 suns), as a larger amount of energy is supplied to the system, but this extra electron flux is not fully harvested in the CO_2 conversion to formate.

Moreover, the potential of the developed system for PEC CO_2 reduction is compared with previous studies conducted by the research group on the electrochemical reduction of CO_2 to formate under relevant current densities ($>$ 90 mA cm^{-2}). The comparison with previous results is carried out using two approaches. In the first case, comparative data of conventional CO_2 electroreduction systems to formate are presented, either using a liquid catholyte (LC) [44,51], or a humidified CO_2 feed in gas phase operation (GC) [5,47,52]. In these cases, the reaction taking place at the anode is the OER with a DSA anode. Additionally, a comparison is made with previous studies focused on reducing the energy consumption of the electrolyzer. In this case, there are two approaches: first, coupling glycerol oxidation (GOR) instead of the OER [53], and second, previous works where photoanodes are integrated to carry out the OER [18]. Both the GOR and PEC studies consider a humidified gas-phase CO_2 feed at the cathode side. Fig. 10 shows the trade-off between the *FE* and *EE* achieved in the different above-mentioned approaches.

This work, with a gas-phase PEC approach using solar concentration, significantly improves the trade-off between production and energy

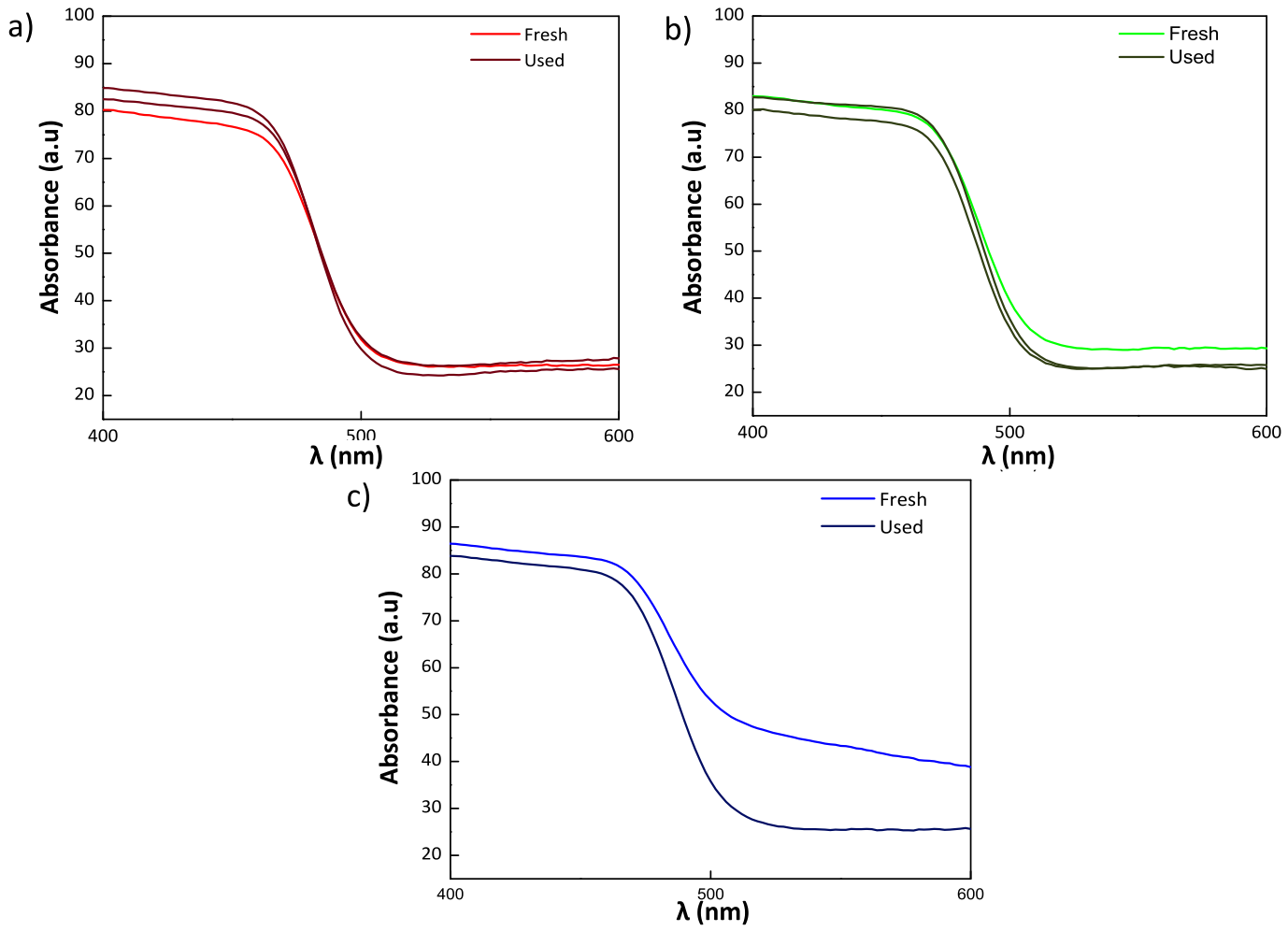

Fig. 8. VIS-absorbance spectra for photoanodes A, B, and C, before and after use. (Red, Photoanode A; Green, Photoanode B; Blue, Photoanode C). (For interpretation of the references to colour in this figure legend, the reader is referred to the web version of this article.)

performance compared to conventional gas phase CO_2 electroreduction systems, achieving *FEs* over 90 % while maintaining higher *EEs*. Conversely, liquid-phase operation can achieve higher *EEs* at lower *FEs* due to reduced cell voltages (3–4.5 V), attributed to an improved conductivity of the liquid catholyte. However, the lower formate production rates and concentrations achieved in liquid-phase configurations, between 2–18 g L^{-1}, disadvantage them as viable solutions compared to the PEC CO_2 conversion developed. Lastly, the coupling of glycerol oxidation in the anode with the electroreduction of CO_2 in the cathode can represent a competitive alternative for enhancing system energy performance, as it leads to higher *EEs*, close to 50 %, as the GOR reduces the anode overpotentials compared to the OER, and it will be part of our future work in PEC systems.

Overall, the results demonstrate the potential of PEC and solar concentration techniques to reduce energy input requirements, offering a pathway toward unbiased PEC CO_2 conversion in industry.

4. Conclusions

Three different photoanode structures are proposed: photoanode A, with a single $BiVO_4$ deposition, photoanode B, with doubled $BiVO_4$ loading by a second deposition, and photoanode C, in which a Bi_2O_3 underlayer improves the FTO-$BiVO_4$ interface, acting as a hole-mirror to reduce the electron-hole recombination. All three photoanode structures have demonstrated remarkable PEC performance for the reduction of CO_2 to formate in gas phase operation. Among these, photoanode C exhibited the highest current density during PEC characterization (–33 mA cm^{-2}) and the highest absorbance in the visible light range. Additionally, its defect-like surface morphology increases the surface area available for the OER, making photoanode C the best alternative for an efficient PEC CO_2 reduction to formate.

Coupling photoanode C with the CO_2 reduction to formate in gas phase at the cathode exhibits excellent results under visible light, as the formate concentration obtained is 59.2 g L^{-1}, with a *FE* of 96 %, meaning that the selectivity of the reaction towards formate is maximized thanks to the extra electron flow provided by light. In this sense, PEC performance increase by around 33 % compared to the conventional dark operation. Furthermore, evaluating the energy requirements in each case reveals, that integrating the illuminated photoanode C alleviates the external bias needed, as the energy consumption is reduced by almost 40 %, achieving a remarkable 317 kWh $kmol^{-1}$. On the other hand, the *EE* is also enhanced to 38 %, mainly thanks to the increase of the *FE* due to the coupling of photoanode C with the CO_2 conversion. In addition, the post-experimental characterization demonstrates the chemical stability of the electrodeposited photoanodes, highlighting this as one of the benefits of this fabrication technique.

Nevertheless, the cell external bias can be further reduced by increasing the incident light with solar concentration. In this case, with photoanode C, there is a notable reduction in the anodic overpotential, which leads to a 10 % energy consumption reduction (290 kW $kmol^{-1}$) when working with 2.5 solar intensity, while maintaining the cathode formate production up to 60 g L^{-1} and 96 % FE. The trade-off between

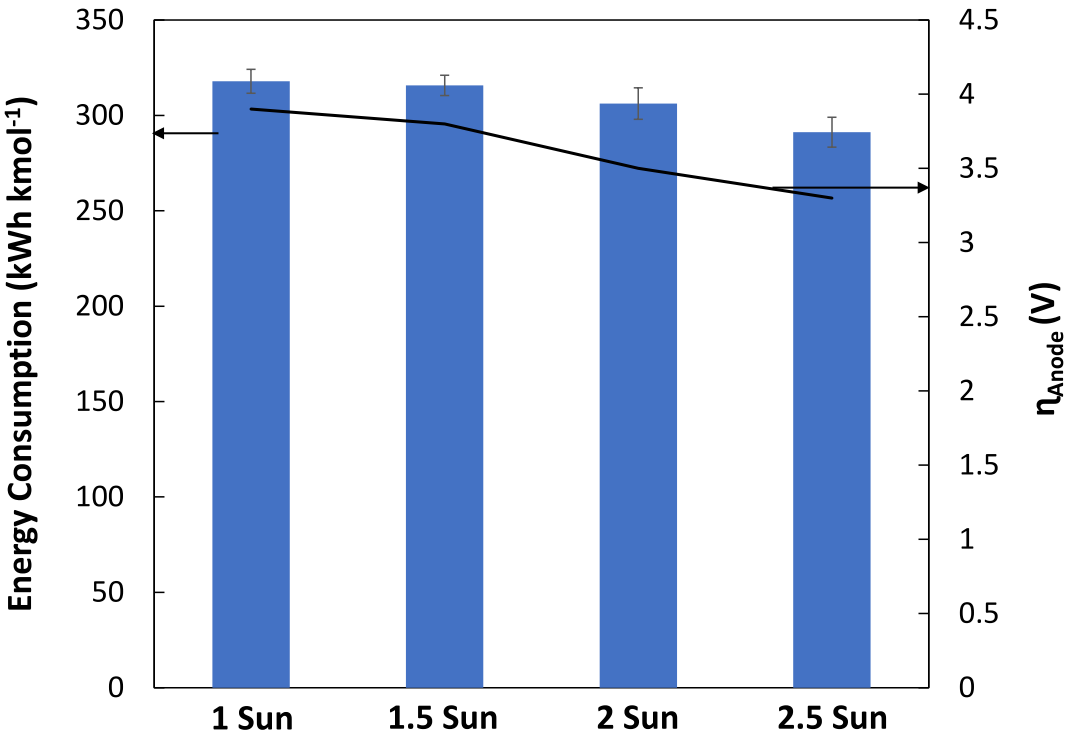

Fig. 9. PEC performance in terms of energy consumption and photoanode overpotential for the continuous CO_2 reduction to formate using photoanode C ($BiVO_4$/Bi_2O_3) at constant j of −29 mA cm^{-2}.

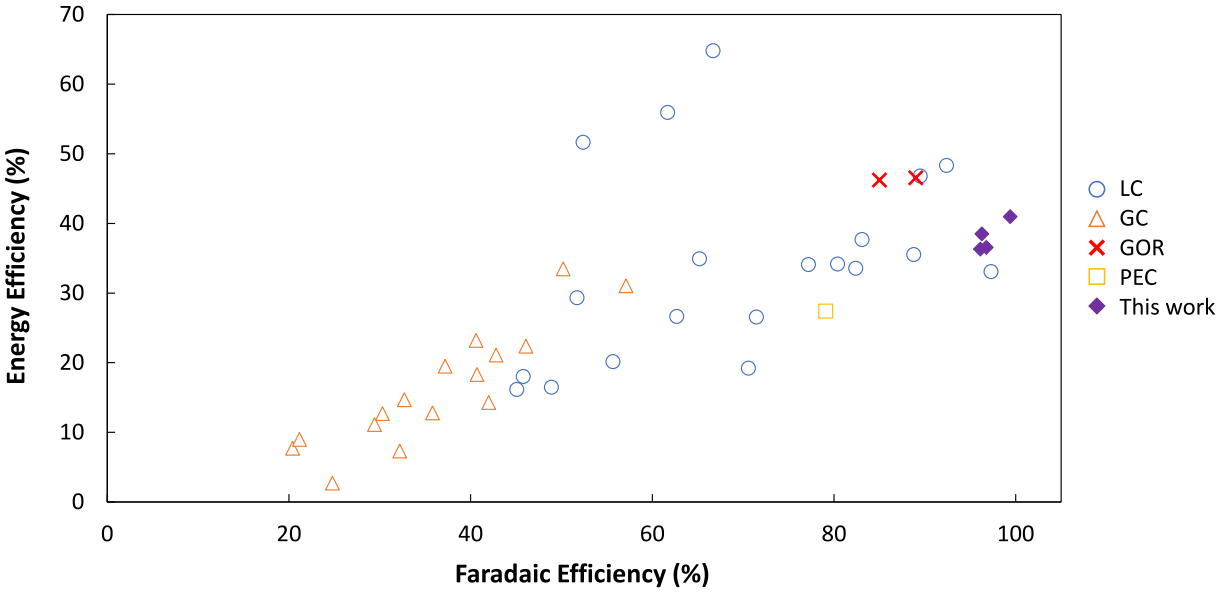

Fig. 10. EE vs FE for electrochemical CO_2 conversion to formate compared with this work (LC, Liquid-phase configuration; GC, gas-phase configuration; GOR, Glycerol Oxidation Reaction; PEC, Photoelectrochemical CO_2 reduction).

FE and *EE* shown by the PEC operation under solar concentration demonstrates the potential for improving the energy management of this alternative compared to the conventional CO_2 electroreduction in gas phase, closing the gap with respect to energy performance that is considered industrially relevant.

All in all, this work continues advancing toward the future scale-up of the CO_2 PEC reduction technology.

CRediT authorship contribution statement

José Antonio Abarca: Writing – original draft, Validation, Methodology, Investigation, Data curation, Conceptualization. **Martí Molera:** Writing – original draft, Methodology, Investigation, Data curation. **Ivan Merino-Garcia:** Writing – review & editing, Validation, Supervision, Methodology, Conceptualization. **Guillermo Díaz-Sainz:** Writing – review & editing, Supervision, Resources, Formal analysis. **Angel Irabien:** Writing – review & editing, Supervision, Funding acquisition, Formal analysis. **José Solla-Gullón:** Writing – review &

editing, Resources, Funding acquisition, Formal analysis. **Cristian Fàbrega:** Writing – review & editing, Supervision, Formal analysis. **Teresa Andreu:** Writing – review & editing, Validation, Resources, Funding acquisition, Formal analysis, Conceptualization. **Jonathan Albo:** Writing – review & editing, Validation, Supervision, Resources, Methodology, Funding acquisition, Formal analysis, Conceptualization.

Declaration of competing interest

The authors declare that they have no known competing financial interests or personal relationships that could have appeared to influence the work reported in this paper.

Acknowledgments

The authors gratefully acknowledge Grant TED2021-129810B-C21 and PLEC2022-009398 funded by MICIU/AEI/10.13039/501100011033/ and by the "European Union NextGenerationEU/PRTR", and Grants PID2022-138491OB-C31, PID2022-138491OB-C32 and PID2022-138491OB-C33 funded by MICIU/AEI/10.13039/501100011033 and by "ERDF/EU". This project has received funding from the European Union's Horizon Europe research and innovation programme under grant agreement No 101118265. Marti Molera acknowledges AGAUR-Generalitat de Catalunya for 2024 FI-1 00421 predoctoral grant. The authors thank Dr. Julià Lopez Vidrier for the access to the UV–vis equipment. Jose Antonio Abarca gratefully acknowledges the predoctoral research grant (FPI) PRE2021-097200. Ivan Merino-Garcia also acknowledges Grant RYC2023-043378-I funded by MICIU/AEI/10.13039/ 501100011033 and by ESF + .

Appendix A. Supplementary data

Supplementary data to this article can be found online at https://doi.org/10.1016/j.cej.2025.163348.

Data availability

Data will be made available on request.

References

[1] Global Greenhouse Gas Overview | US EPA. https://www.epa.gov/ghgemissions/global-greenhouse-gas-overview (accessed September 29, 2024).
[2] A.I. Osman, M. Hefny, M.I.A. Abdel Maksoud, A.M. Elgarahy, D.W. Rooney, Recent advances in carbon capture storage and utilisation technologies: a review, Environ. Chem. Lett. 19 (2021) 797–849, https://doi.org/10.1007/s10311-020-01133-3.
[3] K. Fernández-Caso, G. Díaz-Sainz, M. Alvarez-Guerra, A. Irabien, Electroreduction of CO_2: Advances in the Continuous Production of Formic Acid and Formate, ACS Energy Lett. 8 (2023) 1992–2024, https://doi.org/10.1021/ACSENERGYLETT.3C00489.
[4] M. Rumayor, A. Dominguez-Ramos, P. Perez, A. Irabien, A techno-economic evaluation approach to the electrochemical reduction of CO_2 for formic acid manufacture, J. CO_2 Utili. 34 (2019) 490–499, https://doi.org/10.1016/J.JCOU.2019.07.024.
[5] G. Díaz-Sainz, M. Alvarez-Guerra, B. Ávila-Bolívar, J. Solla-Gullón, V. Montiel, A. Irabien, Improving trade-offs in the figures of merit of gas-phase single-pass continuous CO_2 electrocatalytic reduction to formate, Chem. Eng. J. 405 (2021) 126965, https://doi.org/10.1016/J.CEJ.2020.126965.
[6] C.E. Creissen, M. Fontecave, Solar-Driven Electrochemical CO_2 Reduction with Heterogeneous Catalysts, Adv. Energy Mater. 11 (2021) 2002652, https://doi.org/10.1002/AENM.202002652.
[7] S. Verma, S. Lu, P.J.A. Kenis, Co-electrolysis of CO_2 and glycerol as a pathway to carbon chemicals with improved technoeconomics due to low electricity consumption, Nat. Energy. 4 (2019) 466–474, https://doi.org/10.1038/s41560-019-0374-6.
[8] S. Castro, J. Albo, A. Irabien, Photoelectrochemical Reactors for CO_2 Utilization, ACS Sustain. Chem. Eng. 6 (2018) 15877–15894, https://doi.org/10.1021/ACSSUSCHEMENG.8B03706.
[9] E. Irtem, M.D. Hernández-Alonso, A. Parra, C. Fàbrega, G. Penelas-Pérez, J. R. Morante, T. Andreu, A photoelectrochemical flow cell design for the efficient CO_2 conversion to fuels, Electrochim. Acta. 240 (2017) 225–230, https://doi.org/10.1016/J.ELECTACTA.2017.04.072.
[10] J. Antonio Abarca, G. Díaz-Sainz, I. Merino-Garcia, A. Irabien, J. Albo, Photoelectrochemical CO_2 electrolyzers: From photoelectrode fabrication to reactor configuration, J. Energy Chem. 85 (2023) 455–480, https://doi.org/10.1016/j.jechem.2023.06.032.
[11] B. Endrődi, G. Bencsik, F. Darvas, R. Jones, K. Rajeshwar, C. Janáky, Continuous-flow electroreduction of carbon dioxide, Prog. Energy Combust. Sci. 62 (2017) 133–154, https://doi.org/10.1016/J.PECS.2017.05.005.
[12] B. Liu, T. Wang, S. Wang, G. Zhang, D. Zhong, T. Yuan, H. Dong, B. Wu, J. Gong, Back-illuminated photoelectrochemical flow cell for efficient CO_2 reduction, Nat. Commun. 13 (2022) 7111, https://doi.org/10.1038/S41467-022-34926-X.
[13] P. Chen, Y. Zhang, Y. Zhou, F. Dong, Photoelectrocatalytic carbon dioxide reduction: Fundamental, advances and challenges, Nano. Mat. Sci. 3 (2021) 344–367, https://doi.org/10.1016/J.NANOMS.2021.05.003.
[14] S. Xie, Q. Zhang, G. Liu, Y. Wang, Photocatalytic and photoelectrocatalytic reduction of CO_2 using heterogeneous catalysts with controlled nanostructures, Chem. Commun. 52 (2015) 35–59, https://doi.org/10.1039/C5CC07613G.
[15] P. Mane, I.V. Bagal, H. Bae, A.N. Kadam, V. Burungale, J. Heo, S.W. Ryu, J.S. Ha, Recent trends and outlooks on engineering of $BiVO_4$ photoanodes toward efficient photoelectrochemical water splitting and CO_2 reduction: A comprehensive review, Int. J. Hydrogen Energy. 47 (2022) 39796–39828, https://doi.org/10.1016/J.IJHYDENE.2022.09.146.
[16] W. Jiang, Y. An, Z. Wang, M. Wang, X. Bao, L. Zheng, H. Cheng, P. Wang, Y. Liu, Z. Zheng, Y. Dai, B. Huang, Stress-induced $BiVO_4$ photoanode for enhanced photoelectrochemical performance, Appl. Catal. b. 304 (2022) 121012, https://doi.org/10.1016/j.apcatb.2021.121012.
[17] Y. Fang, D. Commandeur, W.C. Lee, Q. Chen, Transparent conductive oxides in photoanodes for solar water oxidation, Nanoscale Adv. 2 (2020) 626–632, https://doi.org/10.1039/C9NA00700H.
[18] J.A. Abarca, I. Merino-Garcia, G. Díaz-Sainz, M. Perfecto-Irigaray, G. Beobide, A. Irabien, J. Albo, Fabrication and optimization of perovskite-based photoanodes for solar-driven CO_2 photoelectroreduction to formate, Catal. Today. 429 (2024) 114505, https://doi.org/10.1016/j.cattod.2023.114505.
[19] S. Castro, J. Albo, A. Irabien, Continuous conversion of CO_2 to alcohols in a TiO_2 photoanode-driven photoelectrochemical system, J. Chem. Tech. & Biotech. 95 (2020) 1876–1882, https://doi.org/10.1002/jctb.6315.
[20] I. Merino-Garcia, S. Castro, A. Irabien, I. Hernández, V. Rodríguez, R. Camarillo, J. Rincón, J. Albo, Efficient photoelectrochemical conversion of CO_2 to ethylene and methanol using a Cu cathode and TiO_2 nanoparticles synthesized in supercritical medium as photoanode, J. Environ. Chem. Eng. 10 (2022) 107441, https://doi.org/10.1016/j.jece.2022.107441.
[21] J.E. Carrera-Crespo, I. Fuentes-Camargo, R.E. Palma-Goyes, U.M. García-Pérez, J. Vazquez-Arenas, I. Chairez, T. Poznyak, Unrevealing the effect of transparent fluorine-doped tin oxide (FTO) substrate and irradiance configuration to unmask the activity of FTO-$BiVO_4$ heterojunction, Mater. Sci. Semicond. Process. 128 (2021) 105717, https://doi.org/10.1016/j.mssp.2021.105717.
[22] Y. Liang, T. Tsubota, L.P.A. Mooij, R. van de Krol, Highly Improved Quantum Efficiencies for Thin Film $BiVO_4$ Photoanodes, J. Phys. Chem. c. 115 (2011) 17594–17598, https://doi.org/10.1021/jp203004v.
[23] R.-T. Gao, X. Liu, X. Zhang, L. Wang, Steering electron transfer using interface engineering on front-illuminated robust $BiVO_4$ photoanodes, Nano Energy 89 (2021) 106360, https://doi.org/10.1016/j.nanoen.2021.106360.
[24] Z. Li, Z. Xie, W. Li, H.S. Aziz, M. Abbas, Z. Zheng, Z. Su, P. Fan, S. Chen, G. Liang, Charge Transport Enhancement in $BiVO_4$ Photoanode for Efficient Solar Water Oxidation, Mater. 16 (2023) 3414, https://doi.org/10.3390/ma16093414.
[25] J. Xue, J. Li, Q. Bi, C. Tang, L. Zhang, Z. Leng, Yb-substitution triggered BiVO4-Bi2O3 heterojunction electrode for photoelectrocatalytic degradation of organics, Colloids Surf. A Physicochem. Eng. Asp. 593 (2020) 124640, https://doi.org/10.1016/j.colsurfa.2020.124640.
[26] J. Wang, G. Ni, W. Liao, K. Liu, J. Chen, F. Liu, Z. Zhang, M. Jia, J. Li, J. Fu, E. Pensa, L. Jiang, Z. Bian, E. Cortés, M. Liu, Subsurface Engineering Induced Fermi Level De-pinning in Metal Oxide Semiconductors for Photoelectrochemical Water Splitting, Angew. Chem. Int. Ed. 62 (2023) e202217026, https://doi.org/10.1002/anie.202217026.
[27] X. Yao, X. Zhao, J. Hu, H. Xie, D. Wang, X. Cao, Z. Zhang, Y. Huang, Z. Chen, T. Sritharan, The Self-Passivation Mechanism in Degradation of $BiVO_4$ Photoanode, Iscience. 19 (2019) 976–985, https://doi.org/10.1016/j.isci.2019.08.037.
[28] S. Murcia-López, C. Fàbrega, D. Monllor-Satoca, M.D. Hernández-Alonso, G. Penelas-Pérez, A. Morata, J.R. Morante, T. Andreu, Tailoring Multilayered $BiVO_4$ Photoanodes by Pulsed Laser Deposition for Water Splitting, ACS Appl. Mater. Interfaces. 8 (2016) 4076–4085, https://doi.org/10.1021/ACSAMI.5B11698.
[29] Y.-C. Liang, S.-H. Chen, Triangular $BiVO_4$-Bi_2O_3 ultrathin sheet composites for enhancement of photoelectrochemical and photocatalytic performance, J. Sci. Adv. Mater. Devices. 9 (2024) 100730, https://doi.org/10.1016/j.jsamd.2024.100730.
[30] L.C. Mahlalela, C. Casado, J. Marugán, S. Septien, T. Ndlovu, L.N. Dlamini, Synthesis of platelet-like $BiVO_4$ using hyperbranched polyethyleneimine for the formation of heterojunctions with Bi_2O_3, Appl Nanosci. 9 (2019) 1501–1514, https://doi.org/10.1007/s13204-019-00977-8.
[31] Y. Bi, Y. Yang, X.-L. Shi, L. Feng, X. Hou, X. Ye, L. Zhang, G. Suo, J. Chen, Z.-G. Chen, Bi_2O_3/$BiVO_4$@graphene oxide van der Waals heterostructures with enhanced photocatalytic activity toward oxygen generation, J. Colloid. Interface Sci. 593 (2021) 196–203, https://doi.org/10.1016/j.jcis.2021.02.079.
[32] P. Sharma, P. Doiphode, O. Bhorade, A. Yengantiwar, Bismuth vanadate thin films for efficient photoelectrochemical water splitting, Emergent Mater. 3 (2020) 187–194, https://doi.org/10.1007/s42247-020-00093-2.

[33] J. Liu, P. Li, J. Bi, Q. Zhu, B. Han, Design and Preparation of Electrocatalysts by Electrodeposition for CO_2 Reduction, Chem. Eur. J. 28 (2022) e202200242, https://doi.org/10.1002/CHEM.202200242.
[34] C. Martinez Suarez, S. Hernández, N. Russo, $BiVO_4$ as photocatalyst for solar fuels production through water splitting: A short review, Appl. Catal. A Gen. 504 (2015) 158–170, https://doi.org/10.1016/J.APCATA.2014.11.044.
[35] H. Rabiee, L. Ge, X. Zhang, S. Hu, M. Li, Z. Yuan, Gas diffusion electrodes (GDEs) for electrochemical reduction of carbon dioxide, carbon monoxide, and dinitrogen to value-added products: A review, Energy Environ. Sci. 14 (2021) 1959–2008, https://doi.org/10.1039/d0ee03756g.
[36] J.A. Abarca, G. Díaz-Sainz, I. Merino-Garcia, G. Beobide, J. Albo, A. Irabien, Optimized manufacturing of gas diffusion electrodes for CO_2 electroreduction with automatic spray pyrolysis, J. Environ. Chem. Eng. 11 (2023) 109724, https://doi.org/10.1016/J.JECE.2023.109724.
[37] I. Merino-Garcia, E. Alvarez-Guerra, J. Albo, A. Irabien, Electrochemical membrane reactors for the utilisation of carbon dioxide, Chem. Eng. J. 305 (2016) 104–120, https://doi.org/10.1016/J.CEJ.2016.05.032.
[38] M.A. Gaikwad, U.P. Suryawanshi, U.V. Ghorpade, J.S. Jang, M.P. Suryawanshi, J. H. Kim, Emerging Surface, Bulk, and Interface Engineering Strategies on $BiVO_4$ for Photoelectrochemical Water Splitting, Small 18 (2022) 2105084, https://doi.org/10.1002/smll.202105084.
[39] M.M.M. Mostafa, A. Shawky, S.F. Zaman, K. Narasimharao, M. Abdel Salam, A. A. Alshehri, N.H. Khdary, S. Al-Faifi, A.D. Chowdhury, Visible-Light-Driven CO_2 Reduction into Methanol Utilizing Sol-Gel-Prepared CeO_2-Coupled Bi_2O_3 Nanocomposite Heterojunctions, Catalysts 12 (2022) 1479, https://doi.org/10.3390/CATAL12111479/S1.
[40] H. Peng, R.T. Guo, H. Lin, X.Y. Liu, Synthesis of Bi_2O_3/g-C_3N_4 for enhanced photocatalytic CO_2 reduction with a Z-scheme mechanism, RSC Adv. 9 (2019) 37162–37170, https://doi.org/10.1039/C9RA07485F.
[41] L. Liu, Y. Zhang, H. Huang, Junction Engineering for Photocatalytic and Photoelectrocatalytic CO_2 Reduction, Sol. RRL 5 (2021) 2000430, https://doi.org/10.1002/SOLR.202000430.
[42] M. Lamers, S. Fiechter, D. Friedrich, F.F. Abdi, R. Van De Krol, Formation and suppression of defects during heat treatment of $BiVO_4$ photoanodes for solar water splitting, J. Mater. Chem. A Mater. 6 (2018) 18694–18700, https://doi.org/10.1039/c8ta06269b.
[43] J. Quiñonero, R. Gómez, Controlling the amount of co-catalyst as a critical factor in determining the efficiency of photoelectrodes: The case of nickel (II) hydroxide on vanadate photoanodes, Appl. Catal. b. 217 (2017) 437–447, https://doi.org/10.1016/J.APCATB.2017.06.005.
[44] G. Díaz-Sainz, M. Alvarez-Guerra, J. Solla-Gullón, L. García-Cruz, V. Montiel, A. Irabien, CO_2 electroreduction to formate: Continuous single-pass operation in a filter-press reactor at high current densities using Bi gas diffusion electrodes, J. CO_2 Utili. 34 (2019) 12–19, https://doi.org/10.1016/j.jcou.2019.05.035.
[45] W. Deng, P. Zhang, B. Seger, J. Gong, Unraveling the rate-limiting step of two-electron transfer electrochemical reduction of carbon dioxide, Nat. Commun. 13 (2022) 803, https://doi.org/10.1038/s41467-022-28436-z.
[46] S. Wang, T. He, J.H. Yun, Y. Hu, M. Xiao, A. Du, L. Wang, New Iron-Cobalt Oxide Catalysts Promoting $BiVO_4$ Films for Photoelectrochemical Water Splitting, Adv. Funct. Mater. 28 (2018) 1802685, https://doi.org/10.1002/adfm.201802685.
[47] J.A. Abarca, G. Díaz-Sainz, A. Irabien, Inhibiting salt precipitation on the gas diffusion electrode surface in gas-phase CO_2 electroreduction to formate by using an acidic anolyte, J. CO_2 Utili. 86 (2024) 102897, https://doi.org/10.1016/J.JCOU.2024.102897.
[48] Z. Wang, M. Lyu, P. Chen, S. Wang, L. Wang, Energy loss analysis in photoelectrochemical water splitting: a case study of hematite photoanodes, Phys. Chem. Chem. Phys. 20 (2018) 22629–22635, https://doi.org/10.1039/C8CP04021D.
[49] Y. She, Q. Xu, T. Nie, X. Luo, M. Wang, L. Tao, L. Guo, In Situ Investigation of Oxygen Bubble Evolution at Photoanode Surface Affected by Reaction Temperature, J. Phys. Chem. c. 127 (2023) 14197–14210, https://doi.org/10.1021/ACS.JPCC.3C02372.
[50] I. Holmes-Gentle, F.E. Bedoya-Lora, L. Aimone, S. Haussener, Photoelectrochemical behaviour of photoanodes under high photon fluxes, J. Mater. Chem. A Mater. 11 (2023) 23895–23908, https://doi.org/10.1039/D3TA05257E.
[51] G. Díaz-Sainz, K. Fernández-Caso, T. Lagarteira, S. Delgado, M. Alvarez-Guerra, A. Mendes, A. Irabien, Coupling continuous CO_2 electroreduction to formate with efficient Ni-based anodes, J. Environ. Chem. Eng. 11 (2023) 109171, https://doi.org/10.1016/j.jece.2022.109171.
[52] G. Díaz-Sainz, M. Alvarez-Guerra, J. Solla-Gullón, L. García-Cruz, V. Montiel, A. Irabien, Gas–liquid–solid reaction system for CO_2 electroreduction to formate without using supporting electrolyte, AIChE J. 66 (2020) 16299, https://doi.org/10.1002/AIC.16299.
[53] K. Fernández-Caso, A. Peña-Rodríguez, J. Solla-Gullón, V. Montiel, G. Díaz-Sainz, M. Alvarez-Guerra, A. Irabien, Continuous carbon dioxide electroreduction to formate coupled with the single-pass glycerol oxidation to high value-added products, J. CO_2 Utili. 70 (2023) 102431, https://doi.org/10.1016/J.JCOU.2023.102431.